PHYSICAL REVIEW LETTERS **129,** 145901 (2022)

Enhancement and Saturation of Near-Field Radiative Heat Transfer in Nanogaps between Metallic Surfaces

Laura Rincón-García,[1,*] Dakotah Thompson,[2,*,†] Rohith Mittapally,[2] Nicolás Agraït,[1,3,4,‡]
Edgar Meyhofer,[2,§] and Pramod Reddy[2,∥]
[1]*Departamento de Física de la Materia Condensada, Universidad Autónoma de Madrid, E-28049 Madrid, Spain*
[2]*Department of Mechanical Engineering, University of Michigan, Ann Arbor, Michigan 48109, USA*
[3]*Instituto Madrileño de Estudios Avanzados en Nanociencia (IMDEA-Nanociencia), C/Faraday 9, E-28049 Madrid, Spain*
[4]*Condensed Matter Physics Center (IFIMAC) and Instituto Universitario de Ciencia de Materiales "Nicolás Cabrera" (INC),*
Universidad Autónoma de Madrid, E-28049 Madrid, Spain

(Received 27 April 2022; revised 27 May 2022; accepted 8 September 2022; published 29 September 2022)

Near-field radiative heat transfer (NFRHT) between planar metallic surfaces was computationally explored over five decades ago by Polder and van Hove [Phys. Rev. B **4**, 3303 (1971)]. These studies predicted that, as the gap size (d) between the surfaces decreased, the radiative heat flux first increases by several orders of magnitude until d is ~100 nm after which the heat flux saturates. However, despite both the fundamental and practical importance of these predictions, the combined enhancement and saturation of NFRHT at small gaps in metallic surfaces remains experimentally unverified. Here, we probe NFRHT between planar metallic (Pt, Au) surfaces and show that RHT rates can exceed the far-field rate by over a thousand times when d is reduced to ~25 nm. More importantly, we show that for small values of d RHT saturates due to the dominant contributions from transverse electric evanescent modes. Our results are in excellent agreement with the predictions of fluctuational electrodynamics and are expected to inform the development of technologies such as near-field thermophotovoltaics, radiative heat-assisted magnetic recording, and nanolithography.

DOI: 10.1103/PhysRevLett.129.145901

Nanoscale radiative heat transfer [1–3] [also called near-field radiative heat transfer (NFRHT)] is being actively probed [4–13] as novel heat transport phenomena arise when the gap size (d) between a hot planar emitter and a cold planar receiver is reduced to the nanoscale. Such NFRHT phenomena are expected to have strong potential for energy conversion applications [14–20] and thermal management and control [8,10,21]. The pioneering theoretical work of Polder and van Hove [22] suggested that, when the gap size between two planar metallic surfaces is decreased, the radiative heat flux would increase by several orders of magnitude until d becomes comparable to or smaller than the skin depth of the metal [23], after which the heat flux saturates. Past experiments [4,24] on plane-parallel silica surfaces of silica have probed NFRHT in very small gaps (~10 nm) and observed large enhancements over the blackbody limit, however, experimental studies of NFRHT between metallic surfaces have been either limited to larger gap sizes [6] or restricted to nonplanar geometries [12,13,25–28] due to which these interesting and technologically relevant predictions of Polder and van Hove remain experimentally unverified. In this Letter, we perform RHT measurements between plane-parallel surfaces of Pt (and Au) separated by gap sizes <30 nm and demonstrate both large increases in heat flux compared to the far-field as well as saturation of heat currents at small gap sizes. Further, we obtain excellent agreement with fluctuational electrodynamics (FED) calculations.

In our experiments, building upon our past work [24], we employ microfabricated Si-based emitter devices [see Figs. 1(a) and 1(b)] with an integrated Pt serpentine line that acts as both a heater and thermometer. Each emitter features a 15 μm tall circular mesa with a diameter of 80 μm whose surface is coated either with Pt (100 nm thick), Au (100 nm thick), or SiO_2 (2 μm thick) depending on the experiment. Further, we fabricated macroscopic planar receiver devices with doped Si chips coated with the corresponding material (see the Supplemental Material [29] for more details). Cleanliness and planarity of the active region of the device surfaces are critical and hence were carefully characterized through dark-field (DF) optical microscopy and atomic force microscopy (AFM). A DF image of one of the mesas employed is shown in Fig. 1(c) and reveals only one faint particle (see inset). AFM characterization of this same mesa surface [Fig. 1(d)] confirms that the faintly visible particle in the DF image has a height <23 nm (profiles in Fig. S2 in [29]). Furthermore, AFM images of smaller scan areas show that the peak-to-peak roughness of the surface is ~6 nm (see Ref. [29]).

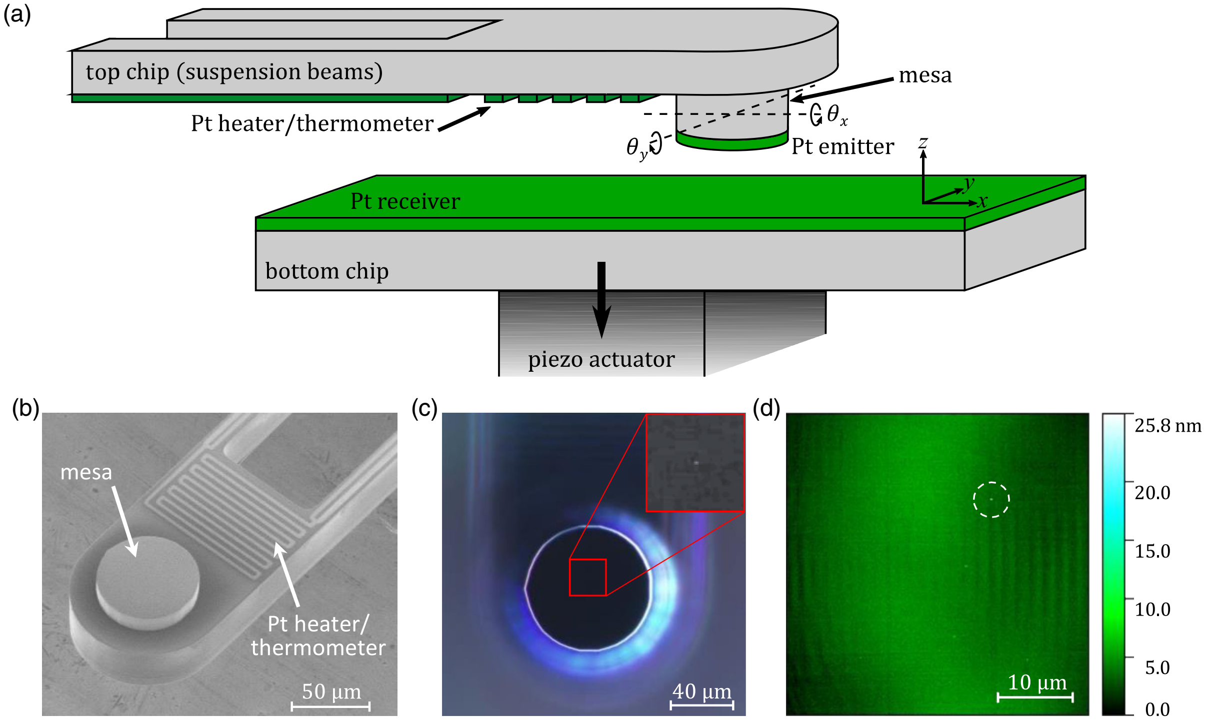

FIG. 1. Experimental setup and devices. (a) Schematic representation of the experimental setup. The bottom chip (made of doped Si coated with Pt, Au, or $\mathrm{SiO_2}$) is placed on a piezoelectric actuator to control the gap size between the bottom chip and a microfabricated emitter coated with the corresponding metal or dielectric. The emitter consists of a round, doped-Si mesa (15 μm tall, 80 μm diameter) protruding from the top chip, and a Pt serpentine used as a heater and thermometer [see also (b)]. θ_x and θ_y represent the tip and tilt angles of the emitter to achieve parallelism with the bottom chip. (b) SEM image of a representative emitter device; the round mesa and the nearby Pt serpentine can be seen. (c) Dark-field image (taken with a 50× Zeiss Epiplan objective) of the mesa surface coated with 100 nm of Pt. The image shows a faint particle almost at the center of the active surface, which can be seen more clearly in the inset (more details in [29]). (d) AFM image of the mesa surface. The faint particle seen in (c) can be see more clearly and is circled (see profiles of the particle in [29]).

To perform NFRHT experiments we employed a custom-built nanopositioner [39] that enables *in situ* control of the parallelism between the devices (with ~6 μrad resolution) as well as the spatial separation between them (~2 nm resolution) in a high-vacuum environment (~10^{-6} Torr) and at room temperature (297 ± 0.5 K). In our measurements, the emitter and receiver devices were integrated into the nanopositioner and the spatial separation between them was controllably changed in the z direction using a piezoelectric actuator on which the receiver was mounted [see Fig. 1(a) and [29] for more details].

To measure the gap dependence of the radiative thermal conductance, the emitter temperature was increased by ~11.6 K by supplying a dc current of 0.9 mA through the integrated Pt serpentine [see Figs. 1(a), 1(b), and 2(a)]. Once the emitter is heated, the piezo actuator is employed to progressively reduce the gap between the devices [Fig. 2(c)] until contact is established following the measurement approach described below. During this process, the heat flux to the receiver [see Fig. 2(b) for a thermal resistance network] varies as a function of gap size and results in a gap-dependent change in the emitter temperature (ΔT_e). This temperature change is monitored by continuously measuring the resistance of the emitter device by superimposing a sinusoidal current of amplitude $I_{ac} = 70\ \mu$A and frequency 497 Hz on the heating dc current in the Pt serpentine and measuring the voltage drop across the serpentine line using an SRS 830 DSP (Stanford Research) dual-phase lock-in amplifier.

The measurement of electrical resistance change, combined with the temperature coefficient of electrical resistance for the Pt heater/thermometer ($1.92 \times 10^{-3}\ \mathrm{K}^{-1}$ from a complementary measurement), enables quantification of ΔT_e with a resolution of ~1 mK in a bandwidth of 0.26 Hz [40]. Figures 2(c) and 2(d) show data from an experiment involving Pt devices where the change in gap size and the corresponding change in the emitter temperature (ΔT_e) can be seen. Upon mechanical contact between the surfaces, the ΔT_e signal changes abruptly to a much larger value, as demonstrated in past work [24], revealing the instant at which contact and conductive heat transfer occur [marked with a red dashed line in Figs. 2(c) and 2(d)]. Note that the gap size at contact is estimated to be ~23 nm, limited by

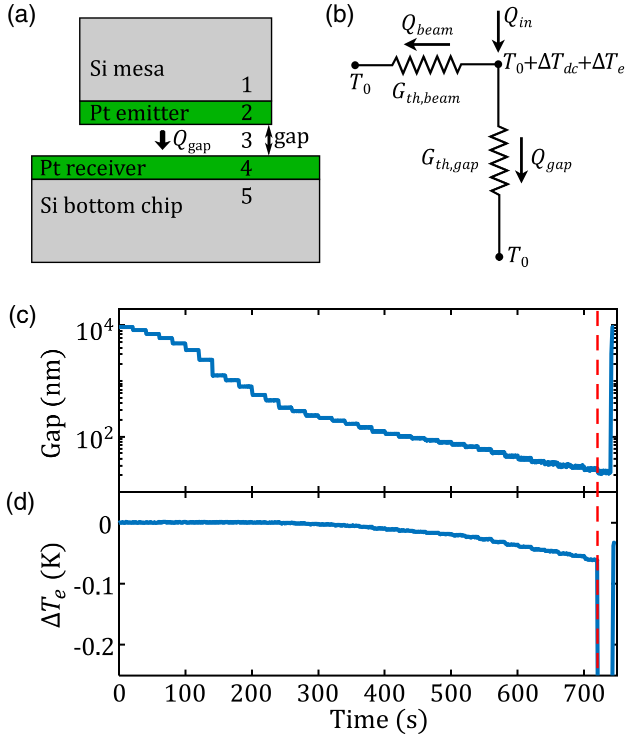

FIG. 2. Heat transfer analysis and measurements. (a) Schematic representation of the experimental system. A heat flux Q_{gap} is established between the hot emitter and the receiver. Numbers 1–5 identify the five layers involved in the RHT analysis. (b) Thermal resistance network showing the main heat transfer pathways. Q_{in} is the heat dissipated in the integrated Pt heater, which heats the emitter to an initial temperature ΔT_{dc} above the room temperature T_0. $G_{\mathrm{th,gap}}$ is the thermal conductance of the gap and $G_{\mathrm{th,beam}}$ is the beam thermal conductance and Q_{beam} is the heat flow through the beams. As the emitter approaches the receiver, Q_{gap} increases and the emitter temperature is reduced by ΔT_e. (c) Gap size between emitter and receiver as a function of time. (d) Measured temperature change of the emitter (ΔT_e) as a function of time. Contact of the emitter with the receiver is signaled by a sudden drop in the emitter temperature, marked with a red dashed line.

the size of the largest particles on the mesa surface [see Fig. S2(e) in [29]].

From the data shown in Fig. 2, we can compute the gap-dependent near-field conductance [$G_{\mathrm{NF}}(d)$] between the two Pt surfaces. Considering the thermal resistance network shown in Fig. 2(b), it can be seen that (see the Supplemental Material, Sec. 2 [29], for details of the derivation)

$$G_{\mathrm{NF}}(d) \sim \frac{Q_{\mathrm{gap}}}{\Delta T_{\mathrm{dc}}} = \frac{Q_{\mathrm{in}} - Q_{\mathrm{beam}}}{\Delta T_{\mathrm{dc}}} = -\frac{\Delta T_e G_{\mathrm{th,beam}}}{\Delta T_{\mathrm{dc}}}, \quad (1)$$

where Q_{gap} is the heat flow through the gap, Q_{in} is the heat input into the emitter per unit time, Q_{beam} is the heat flowing out through the beams, $G_{\mathrm{th,beam}}$ is the thermal conductance of the emitter suspension beams (which is 2.95×10^{-4} WK^{-1}, see Ref. [29]), ΔT_{dc} is the emitter's original temperature above room temperature (11.6 K) at large gap sizes and ΔT_e is the gap-dependent change in the emitter temperature due to the approach of the Pt surfaces. Note that this expression for G_{NF} does not consider the far-field contribution, which is not directly measured in this configuration. From Eq. (1), it can be seen that the gap-dependent ΔT_e enables us to compute the near-field thermal conductance.

The measured $G_{\mathrm{NF}}(d)$ can then be converted to a heat transfer coefficient $h(d) = [G_{\mathrm{th_{gap}}}(d)/A_{\mathrm{mesa}}] = [G_{\mathrm{NF}}(d) + G_{\mathrm{FF}}]/A_{\mathrm{mesa}}$, where A_{mesa} is the area of the emitter mesa ($\sim 5.03 \times 10^{-9}$ m^2), and G_{FF} is the far-field conductance that is determined computationally. Specifically, G_{FF} is calculated considering the gray-body emissivity of Pt (0.054) [41] and then added to the experimental values. The $h(d)$ measured for Pt surfaces is presented in Fig. 3(a) (corresponding data for Au surfaces are presented in Figs. S4 and S5 in [29]). As mentioned above the gap size at contact is assumed to be 23 nm for Pt surfaces, so the data of each measurement is displaced as discussed in our previous work [24].

It can be seen from the measured data that h between Pt surfaces increases dramatically for small gap sizes compared to the far-field regime, reaching a ~1300-fold enhancement in the RHT as the gap size is reduced to ~25 nm. The values observed are also ~65 times larger than the blackbody limit [42]. In addition to the data for the Pt-coated devices, Fig. 3(a) also shows data from measurements of $h(d)$ for SiO$_2$-coated devices, where a 2 μm thick SiO$_2$ layer is thermally grown on otherwise identical emitter and receiver devices. $G_{\mathrm{NF}}(d)$ is measured following the same procedure used for the metallic devices and $h(d)$ is estimated by calculating the G_{FF} for SiO$_2$. It can be seen from these data that the gap-dependence of G_{NF} for Pt- (and Au)-coated devices for $d < 100$ nm is distinctly different from those of SiO$_2$-coated devices and is also much weaker.

To quantitatively compare our experimental results with theory, we modelled the NFRHT for Pt-Pt, Au-Au, and SiO$_2$-SiO$_2$ structures using the framework of FED [22,23,43]. As described in Sec. 4 of the SM [29], we treated our system as a five-layer, one-dimensional structure and computed the total heat transfer coefficient [$h(T,d)$] from

$$h(T,d) = \int_0^\infty \frac{d\omega}{4\pi^2} \frac{\partial[\hbar\omega/(e^{\hbar\omega/k_B T} - 1)]}{\partial T} \times \int_0^\infty k[\tau_s(\omega,k) + \tau_p(\omega,k)]dk, \quad (2)$$

where $\hbar$ is the reduced Planck constant, k_B is the Boltzmann constant, T is the absolute temperature (assumed to be $T = 300$ K), ω is the frequency of the radiation, k is the magnitude of the wave vector component

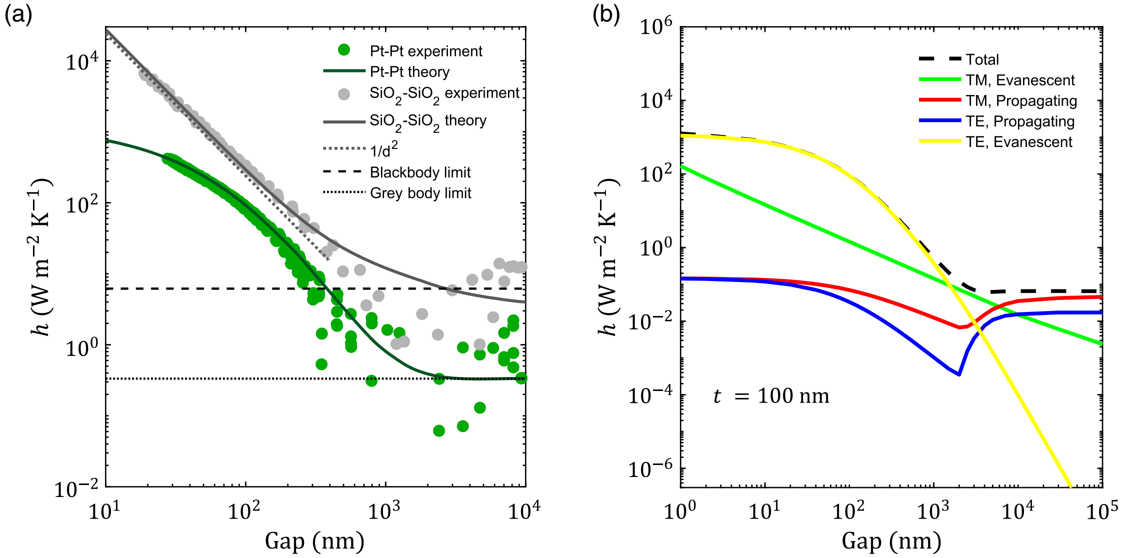

FIG. 3. NFRHT between metallic and polar dielectric surfaces. (a) Gap dependence of the total heat transfer coefficient h measured for Pt (green dots) and SiO_2 surfaces (gray dots), compared with the corresponding theoretical calculations (dark green and gray solid lines, respectively). Experimental data displaced by 26–29 nm for Pt surfaces (from six different measurements) and 19 nm for SiO_2 surfaces (from two different measurements) to account for the smallest achievable gap size. Dashed and dotted horizontal lines are the blackbody and gray body (Pt) limits, respectively, and correspond to the computed far-field value for surfaces with an area equal to that of the mesa and a temperature difference of ~11.6 K. The blackbody limit was computed using a view factor of unity and emissivity of 1, and for the gray body we assumed an emissivity of 0.054 [41] for Pt. The $1/d^2$ dependence (gray dotted line) for SiO_2 surfaces is also shown. (b) Total heat transfer coefficient h as a function of gap size (black dashed line) for the multilayer system in Fig. 2(b) with a Pt coating thickness $t = 100$ nm. The different contributions from TE and TM modes are also shown. Note that below 1 μm gaps the major contribution is from evanescent TE modes.

parallel to the surface planes, and τ_s and τ_p are the transmission probabilities for the transverse electric (TE) and transverse magnetic (TM) modes, respectively. Computational results for Pt- and SiO_2-coated devices are shown in Fig. 3(a) (corresponding data for Au-coated devices are shown in Figs. S4 and S5 in [29]). The data in Fig. 3(a) show that our measurements are in good agreement with the predictions of FED. Further, one can see that our results feature a distinctly different gap dependence between the two materials. In fact, the gap dependence for the SiO_2-coated devices features a $1/d^2$ behavior that corresponds to contributions from surface phonon polaritons, whereas the Pt-coated devices show a much weaker gap dependence with the conductance becoming largely independent of d for small gaps.

To obtain a deeper understanding of the origin of this difference between metals and polar dielectrics, Fig. 3(b) shows results from FED-based calculations where the contributions from evanescent and propagating TE and TM modes are plotted. It can be seen that, in contrast to SiO_2, whose NFRHT is dominated by evanescent TM modes [see Fig. S8 in [29]], the dominant contributions for Pt surfaces are from evanescent TE modes, and similarly for Au surfaces (see Fig. S8 in [29]). We note that in our computational analysis (see Sec. 4 in [29]) we have treated our system as consisting of multiple layers to systematically account for the fact that it employs thin films of Pt or Au. However, a comparison of our computational results for 100-nm-thick films to that of semi-infinite Pt (Au) regions (Fig. S9 in [29]) shows that the magnitude of the computed fluxes is almost identical. From this we can conclude that the 100-nm-thick films act effectively as semi-infinite slabs. Therefore, to understand the underlying physics of the gap dependence of h we examine the RHT between semi-infinite Pt-Pt and Au-Au structures.

In this context it is essential to answer two questions: (i) Why do evanescent TE modes dominate NFRHT in metals as opposed to evanescent TM modes in polar dielectrics? and (ii) why do the contributions of evanescent TE modes saturate with decreasing gap size? In order to directly answer the first question, we show in Figs. 4(a) and 4(b) the frequency- and wave-vector-dependent transmission function corresponding to evanescent TE and TM modes for Pt (Fig. S10 in [29] for Au). It can be seen that, when compared to evanescent TM modes, the transmission for evanescent TE modes is relatively large at low frequencies. In fact, the transmission corresponding to evanescent TM modes is large only at very high frequencies (Fig. S11 in [29]) and is associated with a surface plasmon resonance peak close to the plasma frequency (~1.24×10^{15} Hz for Pt and ~2.17×10^{15} Hz for Au [44]). However, such modes do not make appreciable contributions at room temperature

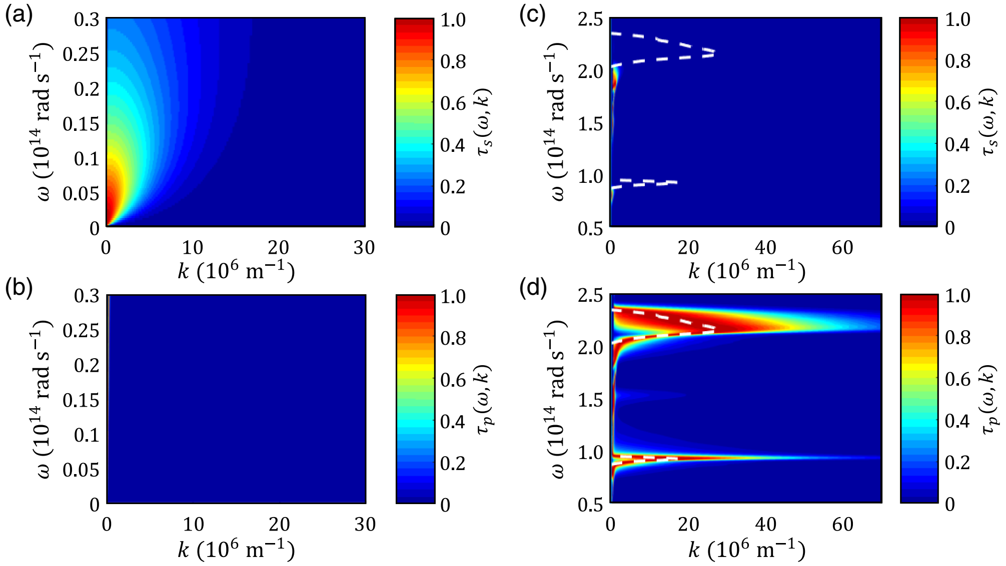

FIG. 4. The transmission probability for metals and polar dielectrics. (a),(b) Transmission probability for evanescent TE (τ_s) and TM modes (τ_p), respectively, as a function of frequency (ω) and magnitude of the parallel wave vector (k) for 100-nm-thick Pt surfaces and a gap size $d = 30$ nm. (c),(d) Transmission probability for evanescent TE (τ_s) and TM modes (τ_p), respectively, as a function of ω and k for 2-μm-thick SiO$_2$ surfaces when $d = 30$ nm. White dashed lines in (c) and (d) correspond to the analytical dispersion relation of the cavity surface phonon polaritons [5,6]. Notice that TE modes make the dominant contribution for Pt-coated devices, while TM modes are clearly dominant for SiO$_2$-coated devices.

due to the $\{\partial[\hbar\omega/(e^{\hbar\omega/k_BT}-1)]/\partial T\}$ term that is present in Eq. (2). In contrast, the computed transmission function for SiO$_2$ [Figs. 4(c) and 4(d)] shows that evanescent TM modes have large values even at low frequencies due to contributions from surface phonon polaritons.

Finally, to understand why the contributions of evanescent TE modes saturate with decreasing gap size, it is instructive to note that past work [22] has shown that the transmission of the evanescent TE modes $[\tau_{s,\mathrm{evan}}(\omega,k)]$ between two semi-infinite half spaces separated by a gap is dependent on the Fresnel reflection coefficients ($r^s_{\mathrm{met,vac}}$) and gap-sizes (d) as follows:

$$\tau_{s,\mathrm{evan}}(\omega,k) \propto \{\mathrm{Im}[r^s_{\mathrm{met,vac}}(\omega,k)]e^{-\gamma''_{\mathrm{vac}}d}\}^2. \qquad (3)$$

Here, $r^s_{\mathrm{met,vac}}(\omega,k)$ is the frequency- and wave-vector-dependent Fresnel reflection coefficient for a TE wave incident from the vacuum onto a metal and

$$\gamma_{\mathrm{vac}} = \gamma'_{\mathrm{vac}} + i\gamma''_{\mathrm{vac}} = \sqrt{\left(\frac{\omega}{c}\right)^2 - k^2}. \qquad (4)$$

It can be seen from Eq. (4) that, for large k, $\gamma''_{\mathrm{vac}} \approx k$ and Eq. (3) simplifies to $\tau_s(\omega,k) \propto \{\mathrm{Im}[r^s_{\mathrm{met,vac}}(\omega,k)]e^{-kd}\}^2$. It is clear from this simplified expression that, as d reduces, modes corresponding to large k vectors also have appreciable transmission values, provided $\mathrm{Im}[r^s_{\mathrm{met,vac}}(\omega,k)]$ does not decrease with increasing k. However, for metals, past theoretical work [23] has shown that there is a cutoff wave vector $k_{\mathrm{cutoff}} \approx \omega_p/c$, where ω_p is the plasma frequency of the metal (Pt/Au in this case) and c is the speed of light in vacuum, above which $\mathrm{Im}[r^s_{\mathrm{met,vac}}(\omega,k)]$ becomes very small. Therefore, the RHT becomes nearly gap independent when d is smaller than a critical distance given by $d_{\mathrm{critical}} \sim (1/k_{\mathrm{cutoff}}) = (c/\omega_p) = (\delta/\sqrt{2})$, where δ is the skin depth for the metal. From this expression and using data from Ref. [44] for ω_p, we estimate a d_{critical} of 30.7 nm for Pt and 17.5 nm for Au, which are consistent with our observations. This explains why saturation of RHT is observed for metallic films, but not for SiO$_2$.

To conclude, we performed systematic experiments of the NFRHT for prototypical metals (Pt/Au) and polar dielectrics (SiO$_2$) and demonstrated that heat transfer rates exceed the far-field and blackbody limits in both cases. Further, we show that gap dependence of NFRHT for metallic surfaces differs significantly from that for polar-dielectric surfaces. Finally, via systematic modeling, we attribute the observed differences to differences in the contributions of evanescent TE and TM modes to NFRHT in metals and polar dielectrics. The experiments provide direct insights into the nature of NFRHT between metallic surfaces.

E. M. and P. R. acknowledge support from DOE-BES through a grant from the Scanning Probe Microscopy Division under Award No. DESC0004871 (Experiments and Analysis) and support from the Army Research Office

Grant No. MURI W911NF-19-1-0279 (fabrication of devices). L. R.-G. acknowledges financial support from the Spanish MECD (Grant No. FPU14/03368 and EST17/00274). N. A. and L. R.-G. acknowledge funding from the Education and Research Council of the Comunidad de Madrid and the European Social Fund (Ref. PEJD-2019-POST/IND-16353) and the Spanish Ministry of Science and Innovation, through Grant No. PID2020–114880 GB-I00.

---

[*] These authors contributed equally to this work.
[†] Present address: Department of Mechanical Engineering, University of Wisconsin, Madison, Wisconsin 53706, USA.
[‡] Corresponding author.
nicolas.agrait@uam.es
[§] Corresponding author.
meyhofer@umich.edu
[∥] Corresponding author.
pramodr@umich.edu

[1] S. A. Biehs, R. Messina, P. S. Venkataram, A. W. Rodriguez, J. C. Cuevas, and P. Ben-Abdallah, Rev. Mod. Phys. **93**, 025009 (2021).
[2] J. C. Cuevas and F. J. Garcia-Vidal, ACS Photonics **5**, 3896 (2018).
[3] B. Song, A. Fiorino, E. Meyhofer, and P. Reddy, AIP Adv. **5**, 053503 (2015).
[4] H. Salihoglu, W. Nam, L. Traverso, M. Segovia, P. K. Venuthurumilli, W. Liu, Y. Wei, W. J. Li, and X. F. Xu, Nano Lett. **20**, 6091 (2020).
[5] B. Song, Y. Ganjeh, S. Sadat, D. Thompson, A. Fiorino, V. Fernández-Hurtado, J. Feist, F. J. Garcia-Vidal, J. C. Cuevas, P. Reddy, and E. Meyhofer, Nat. Nanotechnol. **10**, 253 (2015).
[6] B. Song, D. Thompson, A. Fiorino, Y. Ganjeh, P. Reddy, and E. Meyhofer, Nat. Nanotechnol. **11**, 509 (2016).
[7] R. S. Ottens, V. Quetschke, S. Wise, A. A. Alemi, R. Lundock, G. Mueller, D. H. Reitze, D. B. Tanner, and B. F. Whiting, Phys. Rev. Lett. **107**, 014301 (2011).
[8] V. Fernandez-Hurtado, F. J. Garcia-Vidal, S. H. Fan, and J. C. Cuevas, Phys. Rev. Lett. **118**, 203901 (2017).
[9] M. Ghashami, H. Geng, T. Kim, N. Iacopino, S. K. Cho, and K. Park, Phys. Rev. Lett. **120**, 175901 (2018).
[10] H. Iizuka and S. Fan, Phys. Rev. Lett. **120**, 063901 (2018).
[11] P. Ben-Abdallah and S.-A. Biehs, Phys. Rev. Lett. **112**, 044301 (2014).
[12] L. Worbes, D. Hellmann, and A. Kittel, Phys. Rev. Lett. **110**, 134302 (2013).
[13] A. Kittel, W. Muller-Hirsch, J. Parisi, S. A. Biehs, D. Reddig, and M. Holthaus, Phys. Rev. Lett. **95**, 224301 (2005).
[14] S. Basu, Y. B. Chen, and Z. M. Zhang, Int. J. Energy Res. **31**, 689 (2007).
[15] R. DiMatteo *et al.*, *AIP Conf. Proc.* 738, 42 (2004).
[16] B. Zhao, K. Chen, S. Buddhiraju, G. Bhatt, M. Lipson, and S. Fan, Nano Energy **41**, 344 (2017).
[17] A. Fiorino, L. X. Zhu, D. Thompson, R. Mittapally, P. Reddy, and E. Meyhofer, Nat. Nanotechnol. **13**, 806 (2018).
[18] L. Zhu, A. Fiorino, D. Thompson, R. Mittapally, E. Meyhofer, and P. Reddy, Nature (London) **566**, 239 (2019).
[19] R. Mittapally, B. Lee, L. Zhu, A. Reihani, J. W. Lim, D. Fan, S. R. Forrest, P. Reddy, and E. Meyhofer, Nat. Commun. **12**, 4364 (2021).
[20] C. Lucchesi, D. Cakiroglu, J. P. Perez, T. Taliercio, E. Tournie, P. O. Chapuis, and R. Vaillon, Nano Lett. **21**, 4524 (2021).
[21] C. R. Otey, W. T. Lau, and S. H. Fan, Phys. Rev. Lett. **104**, 154301 (2010).
[22] D. Polder and M. Van Hove, Phys. Rev. B **4**, 3303 (1971).
[23] P. O. Chapuis, S. Volz, C. Henkel, K. Joulain, and J. J. Greffet, Phys. Rev. B **77**, 035431 (2008).
[24] A. Fiorino, D. Thompson, L. X. Zhu, B. Song, P. Reddy, and E. Meyhofer, Nano Lett. **18**, 3711 (2018).
[25] L. Cui, W. Jeong, C. Fernandez-Hurtado, J. Feist, F. J. Garcia-Vidal, J. C. Cuevas, E. Meyhofer, and P. Reddy, Nat. Commun. **8**, 14479 (2017).
[26] K. Kim *et al.*, Nature (London) **528**, 387 (2015).
[27] K. Kloppstech, N. Konne, S. A. Biehs, A. W. Rodriguez, L. Worbes, D. Hellmann, and A. Kittel, Nat. Commun. **8**, 14475 (2017).
[28] S. Shen, A. Mavrokefalos, P. Sambegoro, and G. Chen, Appl. Phys. Lett. **100**, 233114 (2012).
[29] See Supplemental Material at http://link.aps.org/supplemental/10.1103/PhysRevLett.129.145901 for more details on the fabrication of the devices, and Pt surface cleanliness, the thermal characterization of the devices, the near-field thermal conductance of Au-Au devices, the theoretical model employed for modeling NFRHT, the delineation of the contributions of TE, and TM modes to RHT, a discussion of the heat transfer in three-layer systems, the computed transmission probabilities for evanescent modes of the three materials, and the transmission probabilities of metals at very high frequencies, which includes Refs. [30–38].
[30] D. G. Cahill, Rev. Sci. Instrum. **61**, 802 (1990).
[31] A. Fiorino, D. Thompson, L. Zhu, R. Mittapally, S.-A. Biehs, O. Bezencenet, N. El-Bondry, S. Bansropun, P. Ben-Abdallah, E. Meyhofer, and P. Reddy, ACS Nano **12**, 5774 (2018).
[32] S. A. Biehs, E. Rousseau, and J. J. Greffet, Phys. Rev. Lett. **105**, 234301 (2010).
[33] A. Narayanaswamy and Y. Zheng, J. Quant. Spectrosc. Radiat. Transfer **132**, 12 (2014).
[34] S. A. Biehs, Eur. Phys. J. B **58**, 423 (2007).
[35] E. D. Palik, *Handbook of Optical Constants of Solids II* (Academic Press, San Diego, 1998).
[36] C. J. Fu and Z. M. Zhang, Int. J. Heat Mass Transfer **49**, 1703 (2006).
[37] S. Basu, B. J. Lee, and Z. M. Zhang, J. Heat Transf. ASME **132**, 023301 (2010).
[38] S. Basu, B. J. Lee, and Z. M. Zhang, J. Heat Transf. ASME **132**, 023302 (2010).

[39] Y. Ganjeh, B. Song, K. Pagadala, K. Kim, S. Sadat, W. Jeong, K. Kurabayashi, E. Meyhofer, and P. Reddy, Rev. Sci. Instrum. **83**, 105101 (2012).

[40] S. Sadat, E. Meyhofer, and P. Reddy, Rev. Sci. Instrum. **83**, 084902 (2012).

[41] M. F. Modest, *Radiative Heat Transfer*, 3rd ed. (Elsevier Academic Press Inc, San Diego, 2013).

[42] M. Planck, *The Theory of Heat Radiation* (P. Blakiston's Son & Co., Philadelphia, 1914).

[43] S. M. Rytov, Y. A. Kravtsov, and V. I. Tatarskii, *Principles of Statistical Radiophysics* (Springer-Verlag, Berlin; New York, 1987).

[44] M. A. Ordal, R. J. Bell, R. W. Alexander, L. L. Long, and M. R. Querry, Appl. Opt. **24**, 4493 (1985).